Formation mechanism of superconducting phase and its three-dimensional architecture in pseudo-single-crystal $K_xFe_{2-y}Se_2$

Yong Liu[1*], Qingfeng Xing[1], Warren E. Straszheim[1,2], Jeff Marshman[3], Pal Pedersen[4], Richard McLaughlin[5], and Thomas A. Lograsso[1,6]

[1]*Division of Materials Sciences and Engineering, Ames Laboratory, US DOE, Ames, Iowa 50011, USA*

[2]*Materials Analysis and Research Laboratory, Iowa State University, Ames, Iowa 50011, USA*

[3]*Carl Zeiss Microscopy, LLC, Ion Microscopy Innovation Center (IMIC), Peabody, Massachusetts 01960, USA*

[4]*Carl Zeiss Microscopy, LLC, Thornwood, New York 10594, USA*

[5]*Oxford Instruments America, Inc., Concord, Massachusetts 07142, USA*

[6]*Department of Materials Science and Engineering, Iowa State University, Ames, Iowa 50011, USA*

We report how the superconducting phase forms in pseudo-single-crystal $K_xFe_{2-y}Se_2$. I*n situ* scanning electron microscopy (SEM) observation reveals that, as an order-disorder transition occurs, on cooling, most of the high-temperature iron-vacancy-disordered phase gradually changes into the iron-vacancy-ordered phase whereas a small quantity of the high-temperature phase retains its structure and aggregates to the stripes with more iron concentration but less potassium concentration compared to the iron-vacancy-ordered phase. The stripes that are generally recognized as the superconducting phase are actually formed as a remnant of the high-temperature phase with a compositional change after an "imperfect" order-disorder transition. It should be emphasized that the phase separation in pseudo-single-crystal

* Corresponding author: yliu@ameslab.gov

$K_xFe_{2-y}Se_2$ is caused by the iron-vacancy order-disorder transition. The shrinkage of the high-temperature phase and the expansion of the newly created iron-vacancy-ordered phase during the phase separation rule out the mechanism of spinodal decomposition proposed in an early report [Wang et al, Phys. Rev. B **91**, 064513 (2015)]. Since the formation of the superconducting phase relies on the occurrence of the iron-vacancy order-disorder transition, it is impossible to synthesize a pure superconducting phase by a conventional solid state reaction or melt growth. By focused ion beam-scanning electron microscopy, we further demonstrate that the superconducting phase forms a contiguous three-dimensional architecture composed of parallelepipeds that have a coherent orientation relationship with the iron-vacancy-ordered phase.

PACS number(s): 74.70.Xa, 64.75.Nx, 64.70.K-, 81.10.Jt, 81.40.-z

I. INTRODUCTION

In contrast to other iron-based superconductors, $K_xFe_{2-y}Se_2$ superconductors [1] are characteristic of the coexistence of two spatially separated phases, as revealed by x-ray diffraction [2], transmission electron microscopy (TEM) [3], scanning electron microscopy (SEM) [4-5]. The physical properties, phase relations and iron-vacancy order-disorder transition in $A_xFe_{2-y}Se_2$ compounds (A=alkali elements and Tl) have been intensively studied [6-7]. No hole pockets were observed near the Brillouin zone center in the angle-resolved photoemission spectroscopy studies [8-9], which also distinguishes $K_xFe_{2-y}Se_2$ superconductors from other iron-based superconductors. A different pairing symmetry, either *d* wave [10] or *s* wave [11] seems to be responsible for the superconductivity in the compounds.

Despite extensive investigations on $K_xFe_{2-y}Se_2$, the formation mechanism of the superconducting phase in phase-separated $K_xFe_{2-y}Se_2$ superconductors remains unclear. This is critical to the question of whether or not the pure superconducting phase can be synthesized. The superconducting phase was suggested to precipitate from a homogeneous solid solution during the phase separation, i.e. ubiquitous precipitation and growth with decreasing temperature across the tie line in the phase space [5]. The phase separation in $K_xFe_{2-y}Se_2$ had been ascribed to spinodal decomposition later [12]. According to the theory of spinodal decomposition [13-14], the high-temperature iron-vacancy-disordered phase will spontaneously decompose into the superconducting phase and the iron-vacancy-ordered phase below the phase separation temperature. If spinodal decomposition does occur in the phase-separated $K_xFe_{2-y}Se_2$, however, one still can synthesize the pure superconducting phase and the iron-vacancy-ordered phase by adjusting the starting materials out of the miscibility gap between the two phases. By quenching the polycrystalline $K_{2-x}Fe_{4+y}Se_5$ samples in ice water, it was found that the iron-vacancy-ordered phase was absent in the samples by x-ray

diffraction analysis [15]. The superconductivity in the quenched polycrystalline samples was suggested to result from the frozen iron-vacancy-disordered phase [15]. Because the quenching treatment is important to enhance the shielding fraction in magnetization measurement [5], an interesting question arises from whether one can get a bulk superconductor if the high-temperature iron-vacancy-disordered state can be frozen by rapid quenching. In order to gain a better understanding of the previous divergent results, we reexamine the mechanism of the phase separation in single-crystal $K_xFe_{2-y}Se_2$.

In this paper, SEM images are recorded with varying temperature to trace the morphology evolution during the iron-vacancy order-disorder transition in single-crystal $K_xFe_{2-y}Se_2$. We would like to point out that the accurate term "pseudo single crystal" should replace the widely used "single crystal" since the two phases coexist in the sample. Remarkably, neither normal precipitation nor spinodal decomposition catches the essence of the phase separation in the pseudo-single-crystal $K_xFe_{2-y}Se_2$. During the phase separation, the superconducting phase forms as a remnant of the high-temperature phase while most of the high-temperature phase, nearly 90%, is transformed into the iron-vacancy-ordered phase. In an early report by Wang *et al*., a model of hollow truncated octahedron in terms of Archimedean solids for the three-dimensional (3D) microstructure in $K_xFe_{2-y}Se_2$ was conjectured, based on the SEM images obtained in the (001), (110), and (100) surfaces [12]. Having a true 3D structure, however, it is a different matter, and is definitive and newsworthy. By focused ion beam scanning electron microscopy (FIB-SEM), we find that the true 3D microstructure in the pseudo-single-crystal $K_xFe_{2-y}Se_2$ is different from the model constructed by the SEM images taken at different cross sections. The 3D microstructure of the superconducting phase can be more precisely described as incomplete hollow hexahedra.

II. EXPERIMENTAL DETAILS

The pseudo-single-crystals $K_xFe_{2-y}Se_2$ were synthesized with excessive iron additions (z=0, 0.2, and 0.6) in the starting materials $K_{0.8}Fe_{2+z}Se_2$. The crystal growth was performed in a vertical tube furnace at a rate of 6 °C/h cooling down from 1030 to 780 °C [5].

The *in situ* SEM observations were completed on an FEI Quanta-250 scanning electron microscope using backscattered electrons (BSEs). The SEM images were further processed with Photoshop for contrast enhancement: The empty intensity space was removed by level adjustment and the images were Gaussian-blurred by 0.5-1 pixels. The contrast analysis on the original images was performed with Gatan DigitalMicrograph.

The image series for 3D tomography was produced by FIB-SEM using the Carl Zeiss Crossbeam 540 system. The data were reconstructed by use of ORS Visual Advanced SI 3D Visualization software. The Crossbeam 540 is fitted with a NordlysNano electron backscatter diffraction (EBSD) camera from Oxford Instruments. EBSD was performed on the both (001) and (100) plane of the superconducting phase, before collecting images for 3D reconstruction of some volumes. The orientation relationship of the two phases was determined based on Euler anglers of each phase. The crystallographic planes and directions of the parallelepipeds were determined by trace analysis.

III. RESULTS AND DISCUSSION

In situ SEM observation during a heating-cooling cycle was performed in the (001) surface of pseudo-single-crystal $K_xFe_{2-y}Se_2$, as shown in Fig. 1. At room temperature, the minority phase appears bright and forms modulated arrays composed of short isolated stripes. The stripe pattern varies under different heat treatment conditions. The pseudo-single-crystal $K_xFe_{2-y}Se_2$ quenched above the iron vacancy order-disorder transition temperature T_s have the contiguous network throughout the matrix, whereas furnace-cooling obtained crystals have isolated long and thick stripes [5]. The usage of as-grown crystals and those obtained by

quenching treatment yield same results of the evolution of surface morphology with varying temperatures.

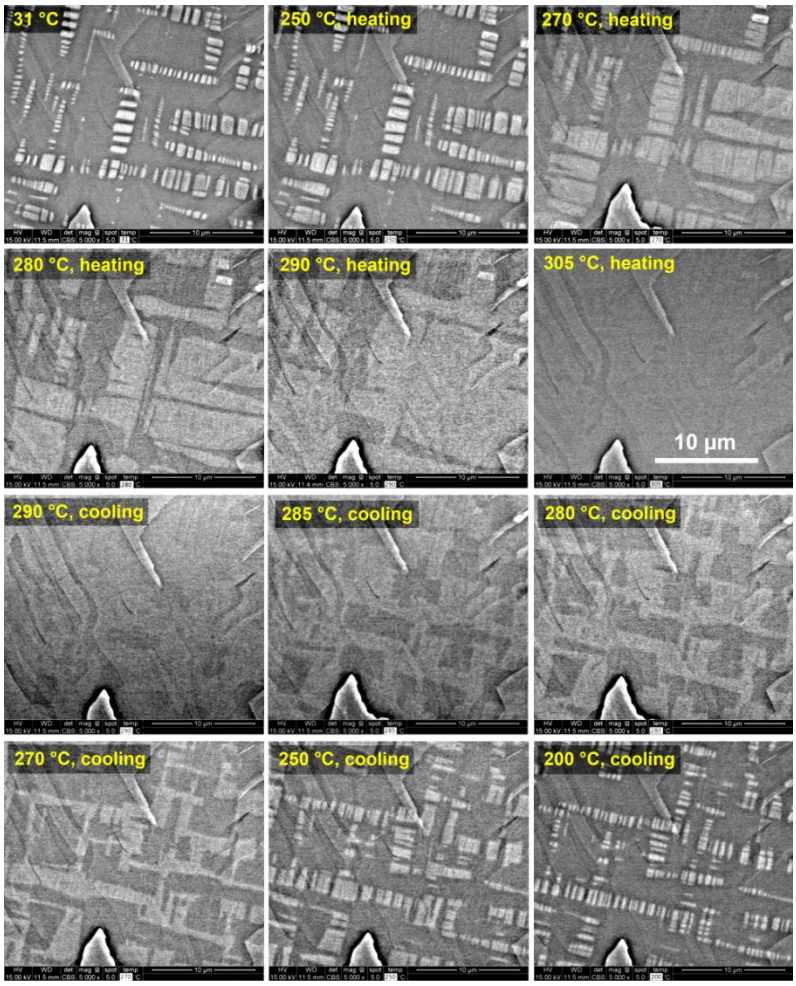

Figure 1. *In situ* SEM BSE images obtained from the (001) plane of pseudo-single-crystal $K_xFe_{2-y}Se_2$, where the stripes and the matrix correspond to the superconducting phase and iron-vacancy-ordered phase, respectively.

With increasing temperature, the stripes coarsen while maintaining their edge and array directions. We see that the area with bright contrast increases and isolated stripes spread and merge into larger ones. The temperature dependence of surface morphology clearly reveals that bright phase increases its fraction at the expense of the matrix. Above 305 °C, the contrast between the two phases completely disappears, which implies that the two phases form a

homogeneous solid solution, a single phase above T_s [5,12]. Upon cooling, the SEM images show the visible contrast at 290 °C. The dark area further increases while bright area shrinks and forms checkerboard pattern at 280 °C. Finally, the bright area aggregates into disconnected stripes. No further microstructure change is observed below 200 °C. The contrast between the bright phases and dark phase becomes small with increasing temperature and gets sharp when temperature decreases. Compared with the initial state before heating, the minority phase at 200 °C on cooling appears smaller than initial and shows different spatial distribution, but retains same edge and array directions. This indicates there is a strong orientation relationship between the two low-temperature phases. The phase changes are only dependent on temperatures and do not proceed over time at a given temperature.

The composition change during the heating and cooling process was simultaneously analyzed by energy dispersive spectroscopy (EDS). As the iron vacancy ordering is involved in the phase formations, the emphasis is placed on the Fe concentration. The superconducting phase is inclined relative to the electron beam direction (see the 3D reconstruction data in this work). To ensure the accurate composition determination, it is necessary to keep the excitation volume and escaping paths of Fe characteristic x-rays within the same material for accurate matrix correction, particularly for the superconducting phase. The accelerating voltage of 8-10 KV was used in this study [16]. The compositions of the stripes and the matrix are listed in Table I. Note an accelerating voltage of 15 kV yield slightly lower iron content in the superconducting phase, which is because the x-ray excitation volume include the both phases. Upon heating, the potassium content increases whereas the iron content decreases in the bright stripes, see Table I. On cooling, the opposite tendency is observed in the bright stripes, where the potassium content decreases whereas the iron content increases. The compositions of the both phases stay unchanged after a heating-cooling cycle. After the two phases merged together on heating, there is no compositional difference between the regions that were

initially different phases.

TABLE I. Composition analysis of the bright stripes and the dark matrix upon heating and cooling. Here, the selenium content is normalized as 2, and both the potassium content and iron content are adhered to the selenium content.

T (°C)	Bright stripe	Dark matrix
25 (heating)	$K_{0.54}Fe_{1.8}Se_2$	$K_{0.75}Fe_{1.53}Se_2$
254 (cooling)	$K_{0.67}Fe_{1.67}Se_2$	$K_{0.76}Fe_{1.57}Se_2$
234 (cooling)	$K_{0.62}Fe_{1.70}Se2$	$K_{0.76}Fe_{1.56}Se_2$
214 (cooling)	$K_{0.63}Fe_{1.70}Se_2$	$K_{0.75}Fe_{1.57}Se_2$

To discuss the microstructure evolution with temperature as observed by SEM, it is necessary to summary the previous structure investigations on the iron vacancy order–disorder transition in $A_xFe_{2-y}Se_2$ compounds (A=alkali elements and Tl) [17-21]. Above T_s, $K_xFe_{2-y}Se_2$ has a $ThCr_2Si_2$-type tetragonal structure with I4/mmm space group, as shown in Fig. 2(a). As the iron vacancy order–disorder transition occurs at a lower temperature, most of high-temperature phase becomes an iron-vacancy-ordered phase, i.e. the matrix phase in Fig. 1. Figure 2(b) shows the unit cell of this vacancy-ordered phase, which corresponds to a $\sqrt{5}\times\sqrt{5}\times 1$ superstructure of original $ThCr_2Si_2$ structure [17-21]. The stripes correspond to the superconducting phase. There is no conclusive knowledge on crystal structure and composition of the superconducting phase because no pure phase has been synthesized. Early scanning tunneling microscope (STM) measurements reported that the superconducting phase is characteristic of a complete FeSe layer and close to the ideal $ThCr_2Si_2$ structure [22-23]. However, another STM work suggested that the superconducting phase consists of a single Fe vacancy for every eight Fe-sites arranged in a $\sqrt{8}\times\sqrt{10}$ parallelogram structure [24]. We also notice that transmission electron microscopy (TEM) measurements found at least three

different Fe-vacancy orders in the FeSe system [25]. It was already reported the superconducting phase may have a potassium-vacancy-ordered $\sqrt{2}\times\sqrt{2}$ superstructure [17,26]. Interestingly, the superconducting phase seems to be mediated by an interface phase, which protects metallic percolative paths in $K_xFe_{2-y}Se_2$ superconductors [27].

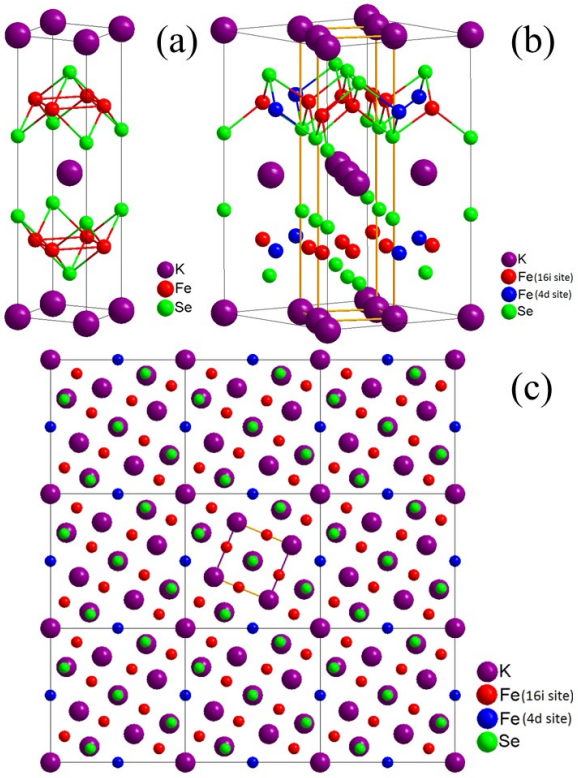

Figure 2. (a) Crystal structure of superconducting phase $K_xFe_2Se_2$ with $ThCr_2Si_2$-type tetragonal structure (I4/mmm), where the potassium atom sites are partially occupied. This structure is identical to that of high-temperature iron-vacancy-disordered phase. But both potassium and iron atom sites are partially occupied in the latter. The potassium and iron vacancy sites are randomly distributed. (b) Crystal structure of iron-vacancy-ordered phase $K_{0.8}Fe_{1.6}Se_2$ with I4/m space group, which is a $\sqrt{5}\times\sqrt{5}\times 1$ superstructure of $ThCr_2Si_2$ structure. The blue balls represent iron vacancy sites (4d), which are completely empty in the iron-vacancy-ordered phase. (c) A diagrammatic representation of (001) plane of the vacancy ordered structure in a $3\times3\times1$ supercell in $K_{0.8}Fe_{1.6}Se_2$, where the iron atoms at 4d sites are

empty and those at 16i are fully occupied. The black solid lines indicate the I4/m unit cell. It should be pointed out that each unit cell of I4/m structure contains a I4/mmm subcell in the center, as shown in Figure (b), where the I4/mmm subcell are marked with orange solid lines.

It is noted that the EBSD pattern from the stripes is identical with that from the matrix (see the Supplementary Materials for details). Therefore, EBSD could not distinguish these two phases. However, this result strongly suggests that the two phases are in very similar crystallographic symmetry groups. For this reason, the $\sqrt{5}\times\sqrt{5}\times 1$ superstructure and $ThCr_2Si_2$ structure are taken for the iron-vacancy-ordered phase and the superconducting phase, respectively. EBSD shows the two phases share the same direction of **c** axis. For the iron-vacancy-ordered phase with the $\sqrt{5}\times\sqrt{5}\times 1$ superstructure, **a**/**b** axes rotate 26.6° from **a**/**b** axes of the superconducting phase with $ThCr_2Si_2$ structure, see Fig. 2(c). Most importantly, if we choose the unit cell based on the $ThCr_2Si_2$ structure for both phases without following the unit cell standardization requirements of a smallest volume with highest symmetry, the two phases also share same directions in the **a** and **b** axes, respectively, with the ion-vacancy-ordered phase having a unit cell larger than the $\sqrt{5}\times\sqrt{5}\times 1$ superstructure. In the following discussion Miller indices and crystal directions are with reference to the minority phase with the $ThCr_2Si_2$ structure.

With knowing the crystal structures and crystallographic orientation relationship between the matrix and stripes in pseudo-single-crystal $K_xFe_{2-y}Se_2$, we continue our discussion on the mechanism of the phase separation revealed in Fig. 1. As can be seen in Fig. 1, the bright phase/superconducting phase increases its volume fraction upon heating but shrinks upon cooling during the iron vacancy order-disorder transition. The change of superconducting phase reflects how the iron vacancy order-disorder transition proceeds in a real time manner. With decreasing temperature, the high-temperature iron-vacancy-disordered phase changes

into an iron-vacancy-ordered phase with a composition of $K_{0.8}Fe_{1.6}Se_2$. It should be pointed out that pseudo-single-crystal $K_xFe_{2-y}Se_2$ can host a small amount of iron impurity atoms ($1.6<2-y<1.8$) during the crystal growth [5]. A small amount of excess iron is essential to synthesize the pseudo-single-crystal $K_xFe_{2-y}Se_2$ with the two separated phases. The excess iron atoms are expelled from the iron-vacancy-ordered phase and aggregate into the superconducting phase, which retains the structure above T_s. On heating the iron–vacancy-ordered matrix changes into an iron–vacancy-disordered state when the temperature is above T_s. Meanwhile, excess iron atoms from the stripes diffuse into the dark matrix phase with lower iron contents. The phase changes described above is supported by the EDS results at various temperatures and is also reflected in the changes in BSE image contrast with temperature, as shown in Fig. 1. Therefore, the phase separation is a diffusion-controlled continuous ordering process. The stripes are the remnant of the high-temperature parent phase after the iron vacancy order-disorder transition.

Our *in situ* observation of the phase separation reveals that the formation of stripes persists nearly within a 100 °C window. In the quenched $K_{2-x}Fe_{4+y}Se_5$ polycrystalline samples, it is possible that the high-temperature iron-vacancy-disordered state can be frozen by quenching at 750 °C in the polycrystalline samples [15]. Such quenched polycrystalline samples without the iron-vacancy-ordered phase could be seen as the pure superconducting phase, where the iron vacancy sites are identical with those occupied sites. T_c of the superconducting phase thus can be tuned by filling the iron vacancies with adding excess iron in the starting materials [15]. It should be pointed out that the quenching treatment only gives rise to a fine modulation of the stripe structure in pseudo-single-crystal $K_xFe_{2-y}Se_2$ [5]. The greatly enhanced shielding fraction in the magnetization measurement results from the contiguous network throughout the matrix by Josephson effect or superconducting proximity effect while the volume fraction of the superconducting phase does not change after the heat

treatment [5]. There is no evidence such as heat capacity data to prove the bulk superconductivity in the quenched polycrystalline samples. It is very likely that the granular superconductivity still dominates those samples, in which there exist too many iron vacancies in the crystal structure compared to the superconducting phase in the pseudo single crystal.

The phase separation induced by the order-disorder transition is consistent with the orientation relationship. The orientation relationship illustrated in Fig. 2(c) clearly shows only atomic ordering through atomic diffusion is needed for the phase separation. Our observations exclude spinodal decomposition mechanism for the phase separation in pseudo-single-crystal $K_xFe_{2-y}Se_2$ as previously suggested [12]. The initial stage is crucial to judge whether the spinodal decomposition or normal nucleation and growth happened to the sample. If spinodal decomposition really happens, the interface between the stripes and matrix should be initially very diffuse but sharpen gradually on cooling. Neither the shrinkage of the parent phase nor the expansion of the new phase can be observed during the spinodal decomposition [13-14]. On the other hand, the spinodal decomposition shall proceed with time at the temperature below the spinodal point based on the characteristics of the phase diagram. In contrast, the current work shows the phase changes are only dependent on temperatures and do not change over time at a given temperature below T_s.

SEM images shown in Fig. 1 only provide the two-dimensional (2D) spatial distribution of the stripes in (001) plane of pseudo-single-crystal $K_xFe_{2-y}Se_2$. Three-dimensional spatial distribution of the stripes in the matrix was reconstructed through a series of SEM micrographs obtained by successively cross sectioning by FIB-SEM. It should be pointed out that the 3D microstructure of the stripes in $Rb_xFe_{2-y}Se_2$ single crystals had been reconstructed in a volume of $10\times7.5\times0.8$ μm^3 by FIB-SEM [28]. It was found that the stripes consist of discontinuous plates aligned along the {113} habit planes in the $Rb_xFe_{2-y}Se_2$ single crystals [28]. In this study, volumes up to $16\times10\times10$ μm^3 (16×10 μm^2 for the cross section and 10 μm

along slicing direction) were reconstructed. In contrast to the discontinuous plates observed in $Rb_xFe_{2-y}Se_2$ samples, the stripes in $K_xFe_{2-y}Se_2$ samples form a contiguous 3D architecture.

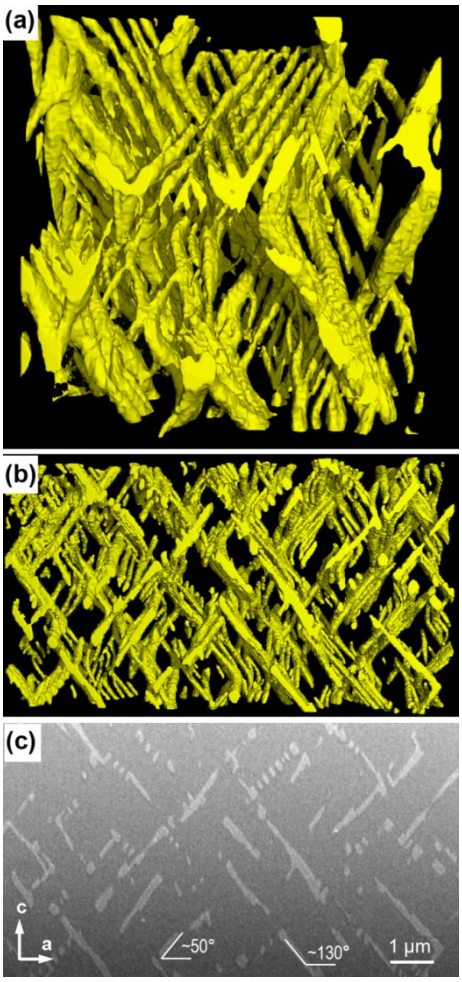

Figure 3. (a) Reconstructed 3D morphology of the stripe phase in the pseudo-single-crystal $K_xFe_{2-y}Se_2$ with a volume of 2×2×2 μm^3. (b) (010) plane view of the stripe phase in a reconstructed volume of about 10×6×2 μm^3. (c) A raw image of (010) plane used for 3D reconstruction of the volume shown in (b).

In Figs. 3(a) and (b), the screen shots display the typical features of 3D microstructure (see more details in the attached movies). As we observe along **c** axis, the snapshots exhibit a square-bowl-like structure. The stripes lie within the four tilted planes of the square bowl. As

the $K_xFe_{2-y}Se_2$ single crystals were cleaved along the *ab* plane, we actually observed the network that corresponds to the cross section of the superconducting phase that is elongated in 3D structure. When we observe along **a** or **b** axis, the microstructure shows a parallelogram shape. The 3D architecture is composed of interlacing branches of the stripes. Consistent with what is observed along the **c** axis, the stripes do lie in different planes. In each plane, the stripes orient nearly parallel to each other. The stripes have a length of several micrometers in this plane. Then the stripes twist, bend, furcate and grow into its adjacent planes. Indirect measurements such as NMR [29], muon spin rotation (μSR) [30], and Mössbauer [31-32] spectroscopy have revealed nearly 90% of the sample volumes exhibit large-moment antiferromagnetic (AFM) order, while 10% of the sample volumes remain paramagnetic (PM) and attributed to a metallic/superconducting phase in $A_xFe_{2-y}Se_2$ single crystals. In this study, we directly obtain that the volume fraction of superconducting phase is between 10.2% and 11.5%, which well matches the previous results.

Our direct observation reveals that the stripes observed in 2D actually wrap the matrix and are parallelepipeds. There are two parameters for an orientation relationship in the 3D microstructure of pseudo-single-crystal $K_xFe_{2-y}Se_2$, i.e. the growth habit plane of superconducting phase and directions of the stripes. Speller *et al*. have pointed out that the superconducting phase forms with {113} habit planes [4,28]. According to EBSD and 3D reconstruction results, the superconducting phase appears as parallelepipeds with two side surfaces parallel to two {113} planes and the longitude direction parallel to the <301> direction which is the interception line of the two {113} planes, as illustrated in Fig. 4. In addition, the parallelepipeds lie in a {113} plane, change their directions within the {113} plane, branch, and bend into another {113} plane. The overall 3D arrangement of the parallelepipeds appears to form incomplete hollow hexahedra, rather than hollow truncated octahedral Archimedean solids as speculated from 2D images [12].

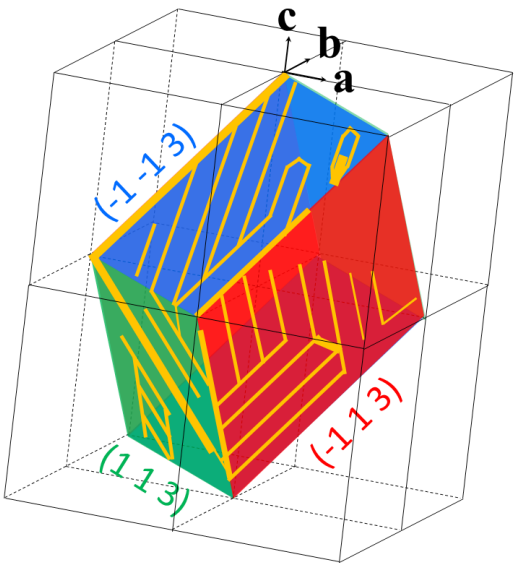

Figure 4. Schematic drawing of the 3D architecture of the superconducting phase: parallelepipeds with {113} planes and along <301> directions.

IV. CONCLUSIONS

In summary, we have shown that the formation of the superconducting phase is driven by the iron vacancy order-disorder transition in pseudo-single-crystal $K_xFe_{2-y}Se_2$. The superconducting phase is the remnant of high-temperature phase with compositional changes. It is difficult to obtain the superconducting phase without the occurrence of the iron vacancy order-disorder transition. Our results strongly suggest that it is impossible to synthesize the pure superconducting phase by the conventional solid state reaction or flux growth. We have provided complete pictures of the 3D morphology and crystallographic characteristics of the superconducting phase and of the orientation relationship between the two phases. The superconducting phase forms a contiguous 3D architecture with incomplete parallelepipeds of {113} side planes and elongates along <301> directions. The two phases share same **c**-axis direction and have a rotation of 26.6° relative to each other. Clarification of the 3D

morphology and the crystallographic orientation relationship between the two phases should make a solid foundation for a future theoretical modelling.

Acknowledgments

This work was supported by the U.S. Department of Energy (DOE), Office of Science, Basic Energy Sciences, Materials Science and Engineering Division. The research was performed at Ames Laboratory, which is operated for the U.S. DOE by Iowa State University under contract # DE-AC02-07CH11358.

References

1. J. G. Guo, S. F. Jin, G. Wang, S. C. Wang, K. X. Zhu, T. T. Zhou, M. He, and X. L. Chen, Phys. Rev. B **82**, 180520(R) (2010).
2. A. Ricci, N. Poccia, G. Campi, B. Joseph, G. Arrighetti, L. Barba, M. Reynolds, M. Burghammer, H. Takeya, Y. Mizuguchi, Y. Takano, M. Colapietro, N. L. Saini, and A. Bianconi, Phys. Rev. B **84**, 060511(R) (2011).
3. Z. Wang, Y. J. Song, H. L. Shi, Z. W. Wang, Z. Chen, H. F. Tian, G. F. Chen, J. G. Guo, H. X. Yang, and J. Q. Li, Phys. Rev. B **83**, 140505(R) (2011).
4. S. C. Speller, T. B. Britton, G. M. Hughes, A. Krzton-Maziopa, E. Pomjakushina, K. Conder, A. T. Boothroyd, and C. R. M. Grovenor, Supercond. Sci. Technol. **25**, 084023 (2012).
5. Y. Liu, Q. Xing, K. W. Dennis, R. W. McCallum, and T. A. Lograsso, Phys. Rev. B **86**, 144507 (2012).
6. E. Dagotto, Rev. Mod. Phys. **85**, 849 (2013).
7. W. Bao, J. Phys.: Condens. Matter **27**, 023201 (2015).
8. T. Qian, X.-P. Wang, W.-C. Jin, P. Zhang, P. Richard, G. Xu, X. Dai, Z. Fang, J.-G. Guo, X.-L. Chen, and H. Ding, Phys. Rev. Lett. **106**, 187001 (2011).
9. Y. Zhang, L. X. Yang, M. Xu, Z. R. Ye, F. Chen, C. He, H. C. Xu, J. Jiang, B. P. Xie, J. J. Ying, X. F. Wang, X. H. Chen, J. P. Hu, M. Matsunami, S. Kimura, and D. L. Feng, Nat. Mater. **10**, 273 (2011).
10. T. A. Maier, S. Graser, P. J. Hirschfeld, and D. J. Scalapino, Phys. Rev. B **83**, 100515(R) (2011).
11. T. Saito, S. Onari, and H. Kontani, Phys. Rev. B **83**, 140512(R) (2011).
12. Z. Wang, Y. Cai, Z. W. Wang, C. Ma, Z. Chen, H. X. Yang, H. F. Tian, and J. Q. Li, Phys. Rev. B **91**, 064513 (2015).

13. J. W. Christian, *The Theory of Transformations in Metals and Alloys* (Part I + II), 3rd edition, Pergamon Press, Oxford (2002).
14. D. A. Porter and K. E. Easterling, *Phase Transformations in Metals and Alloys*, 2nd edition, Chapman & Hall, London (1992).
15. C.-H. Wang, T.-K. Chen, C.-C. Chang, C.-H. Hsu, Y.-C. Lee, M.-J. Wang, P. M. Wu, and M.-K. Wu, Europhys. Lett. **111**, 27004 (2015).
16. Monte Carlo simulation by CASINO [D. Drouin, A. R. Couture, D. Joly, X. Tastet, V. Aimez, and R. Gauvin, Scanning **29,** 92 (2011)] shows that the Fe Kα X-ray excitation volume is less than 140 nm in depth and 70 nm in lateral radius at an acceleration voltage of 8 kV for $K_{0.54}Fe_{1.8}Se_2$. The excitation volumes for K Kα and Se L_{III} X-rays are less than 500 nm in depth and 200 nm in radius.
17. A. Ricci, N. Poccia, B. Joseph, G. Arrighetti, L. Barba, J. Plaisier, G. Campi, Y. Mizuguchi, H. Takeya, Y. Takano, and N. L. Saini, Supercond. Sci. Technol. **24**, 082002 (2011).
18. W. Bao, Q. Z. Huang, G. F. Chen, M. A. Green, D. M. Wang, J. B. He, and Y. M. Qiu, Chin. Phys. Lett. **28**, 086104 (2011).
19. V. Yu. Pomjakushin, D. V. Sheptyakov, E. V. Pomjakushina, A. Krzton-Maziopa, K. Conder, D. Chernyshov, V. Svitlyk, and Z. Shermadini, Phys. Rev. B **83**, 144410 (2011).
20. D. P. Shoemaker, D. Y. Chung, H. Claus, M. C. Francisco, S. Avci, A. Llobet, and M. G. Kanatzidis, Phys. Rev. B **86**, 184511 (2012).
21. S. V. Carr, D. Louca, J. Siewenie, Q. Huang, A. Wang, X. Chen, and P. Dai, Phys. Rev. B **89**, 134509 (2014).
22. W. Li, H. Ding, P. Deng, K. Chang, C. Song, K. He, L. Wang, X. Ma, J.-P. Hu, X. Chen, and Q.-K. Xue, Nat. Phys. **8**, 126 (2012).

23. W. Li, H. Ding, Z. Li, P. Deng, K. Chang, K. He, S. Ji, L. Wang, X. Ma, J.-P. Hu, X. Chen, and Q.-K. Xue, Phys. Rev. Lett. **109**, 057003 (2012).

24. X. Ding, D. Fang, Z. Wang, H. Yang, J. Liu, Q. Deng, G. Ma, C. Meng, Y. Hu, and H.-H. Wen, Nat. Commun. **4**, 1897 (2013).

25. T.-K. Chen, C.-C. Chang, H.-H. Chang, A.-H. Fang, C.-H. Wang, W.-H. Chao, C.-M. Tseng, Y.-C. Lee,c, Y.-R. Wu, M.-H. Wen, H.-Y. Tang, F.-R. Chen, M.-J. Wang, M.-K. Wu, and D. V. Dyck, Proc. Natl. Acad. Sci. USA 111, 63 (2014).

26. Z.-W. Wang, Z. Wang, Y.-J. Song, C. Ma, Y. Cai, Z. Chen, H.-F. Tian, H.-X. Yang, G.-F. Chen, and J.-Q. Li, J. Phys. Chem. C **116**, 17847 (2012).

27. A. Ricci, N. Poccia, B. Joseph, D. Innocenti, G. Campi, A. Zozulya, F. Westermeier, A. Schavkan, F. Coneri, A. Bianconi, H. Takeya, Y. Mizuguchi, Y. Takano, T. Mizokawa, M. Sprung, and N. L. Saini, Phys. Rev. B 91, 020503(R) (2015).

28. S. C. Speller, P. Dudin, S. Fitzgerald, G. M. Hughes, K. Kruska, T. B. Britton, A. Krzton-Maziopa, E. Pomjakushina, K. Conder, A. Barinov, and C. R. M. Grovenor, Phys. Rev. B **90**, 024520 (2014).

29. Y. Texier, J. Deisenhofer, V. Tsurkan, A. Loidl, D. S. Inosov, G. Friemel, and J. Bobroff, Phys. Rev. Lett. **108**, 237002 (2012).

30. Z. Shermadini, H. Luetkens, R. Khasanov, A. Krzton-Maziopa, K. Conder, E. Pomjakushina, and H-H. Klauss, A. Amato, Phys. Rev. B **85**, 100501(R) (2012).

31. D. H. Ryan, W. N. Rowan-Weetaluktuk, J. M. Cadogan, R. Hu, W. E. Straszheim, S. L. Bud'ko, and P. C. Canfield, Phys. Rev. B **83**, 104526 (2011).

32. V. Ksenofontov, G. Wortmann, S. A. Medvedev, V. Tsurkan, J. Deisenhofer, A. Loidl, and C. Felser, Phys. Rev. B **84**, 180508(R) (2011).

Supplemental Material

Formation mechanism of superconducting phase and its three-dimensional architecture in pseudo-single-crystal $K_xFe_{2-y}Se_2$

Yong Liu*, Qingfeng Xing[1], Warren E. Straszheim[1,2], Jeff Marshman[3], Pal Pedersen[4], Richard McLaughlin[5], and Thomas A. Lograsso[1,6]

[1]*Division of Materials Sciences and Engineering, Ames Laboratory, U.S. DOE, Ames, Iowa 50011, USA*

[2]*Materials Analysis and Research Laboratory, Iowa State University, Ames, Iowa 50011, USA*

[3]*Carl Zeiss Microscopy, LLC, Ion Microscopy Innovation Center (IMIC), Peabody, Massachusetts 01960, USA*

[4]*Carl Zeiss Microscopy, LLC, Thornwood, New York 10594, USA*

[5]*Oxford Instruments America, Incorporated, Concord, Massachusetts 07142, USA*

[6]*Department of Materials Science and Engineering, Iowa State University, Ames, Iowa 50011, USA*

* E-mail: yliu@ameslab.gov

1. Orientation relationship determination by EBSD

Electron backscatted diffraction (EBSD) is used to determine the crystallographic orientation relationship of the majority (matrix) and minority (stripe) phases. The crystallographic structural data of the two phases are from Ref. [S1] and are shown in Tables S1 and S2 below.

Table S1. Crystallographic structural data of the majority phase with I4/m symmetry (space group # 87). *a* = 8.72659 Å, *c* = 14.11929 Å. Stoichiometry: $K_{0.8}Fe_{1.44}Se_2$.

Atom	Site	x	y	z	U_{iso}*100/Å^2	Occupancy
K	8h	0.1185	0.7112	0.5	3.34	0.746
K	2a	0	0	0	3.34	1.030
Fe	16i	0.1037	0.1946	0.2577	0.48	0.801
Fe	4d	0.5	0	0.25	0.48	0.397
Se	16i	0.1026	0.7042	0.14527	1.98	1
Se	4e	0	0	0.36404	1.54	1

Table S2. Crystallographic structural data of the minority phase (superconducting phase) with I4/mmm symmetry (space group #139). *a* = 3.82803 Å, *c* = 14.2634 Å. Stoichiometry: $K_{0.545}Fe_1Se_2$.

Atom	Site	x	y	z	U_{iso}*100/Å^2	Occupancy
K	2a	0	0	0	2	0.545
Fe	4d	0	0.5	0.25	1	1.001
Se	4e	0	0	0.35773	1.82	1

The majority phase and minority phase shows identical experimental EBSD patterns. This is further confirmed by dynamic simulation and checking the cross correlation factor of the simulated patterns of the two phases (courtesy of A. Winkleman from Bruker AXS Inc.). However, sometimes it appears that there was a slight pattern rotation between the two neighboring phases, when EBSD was performed on a cleaved (0 0 1) surface and the minority phase is larger than one micrometers. In fact, the pattern rotation is caused by the height difference formed during cleavage, as visible in SEM images with pits that is formed after the minority phase was pulled off. No pattern rotation was observed when EBSD was performed on a flat surface milled by FIB.

Raw EBSD patterns were collected from a map and processed offline for orientation determination. To avoid orientation errors caused by trapezium and trapezoidal distortions [S2], only phases from neighboring regions were chosen for orientation relationship determination, as shown in Figs. S1 and S2.

The current commercial EBSD software only gives Euler angles of a phase to describe the rotation frp, the sample frame to the crystal reference frame. We developed Eq. 1 to calculate the coordinate transformation matrix $\left|M^*\right|$ to find the pairs of parallel directions or

planes. $\lfloor M^* \rfloor$ converts the vector $\mathbf{K}_P$ with respect to the unit cell of the majority phase P to the corresponding vector $\mathbf{K}_S$ with respect to the unit cell of the minority phase S, namely, $\mathbf{K}_S = \lfloor M^* \rfloor \mathbf{K}_P$.

$$\lfloor M^* \rfloor = \lfloor T_S \rfloor^{-1} \lfloor g_S \rfloor \lfloor g_P \rfloor^{-1} \lfloor T_P \rfloor, \quad (1)$$

where $\lfloor g_S \rfloor$ and $\lfloor g_P \rfloor$ are passive orientation matrices for minority phase and the majority phase, respectively, and $\lfloor T_S \rfloor$ and $\lfloor T_P \rfloor$ are the coordinate transformation matrices that transform the fractional coordinate system to Cartesian crystal reference frame for the minority and majority phases, respectively. $\lfloor g_S \rfloor$ and $\lfloor g_P \rfloor$ can be calculated using the following formula for Bunge's Euler angles ϕ1, Φ, and ϕ2 that are provided by EBSD software. $\lfloor T_S \rfloor$ and $\lfloor T_P \rfloor$ are determined the crystal lattice parameters and how the crystal reference frames are established from the crystal basis.

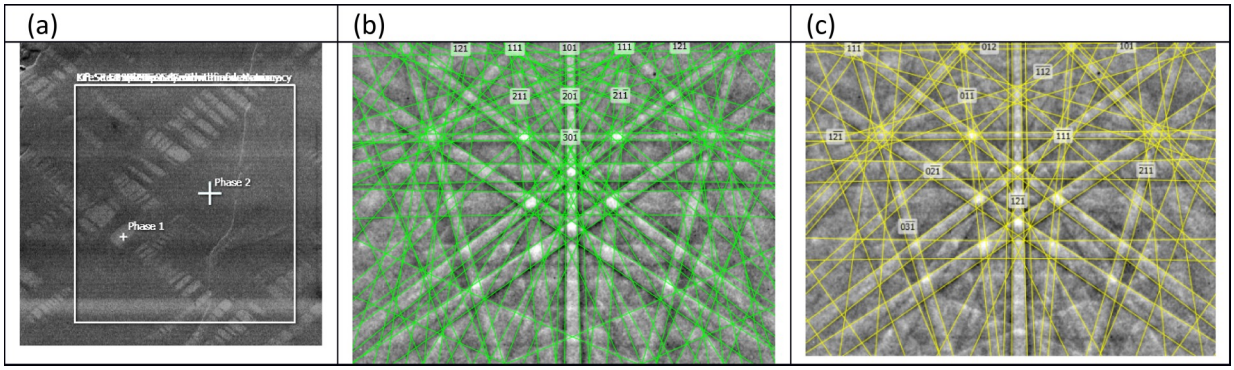

Figure S1. EBSD analysis on a cleaved (0 0 1) surface for both phases: (a) data acquisition map in the framed region, (b) indexed EBSD pattern from the minority phase (Phase 1) as indicated in (a), and (c) indexed EBSD pattern from the majority phase (Phase 2) as indicated in (a). The vertical central band in (b) is along the projected [0 1 0] of the minority phase. The band was used to align the crystal before image acquisition for 3D reconstruction by FIB-SEM. The Euler angles for the two phases are (165.5°, 172.1°, 75.7°) and (165.0°, 172.6°, 11.8°) for the minority phase and the majority phase, respectively.

(a)	(b)	(c)

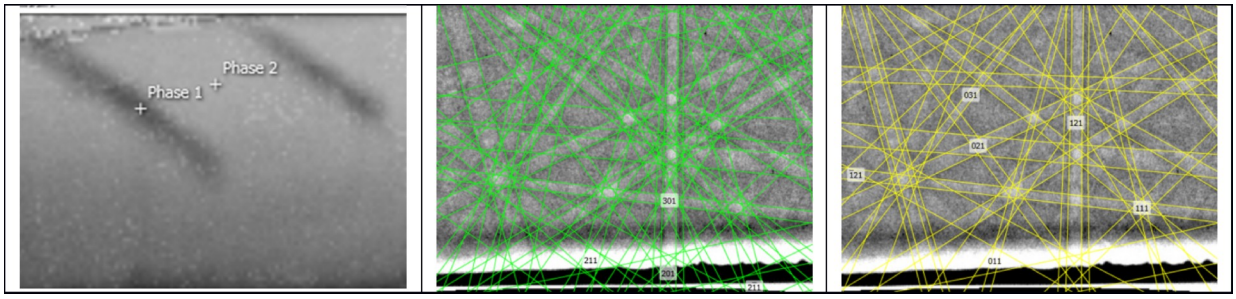

Figure S2. EBSD analysis on a cross-section surface milled with a 30 kV Ga ion beam and polished with a 5 kV Ga ion beam. (a) data acquisition map, (b) indexed EBSD pattern from the minority phase (Phase 1) as indicated in (a), and (c) indexed EBSD pattern from the majority phase (Phase 2) as indicated in (a). The Euler angles for the two phases are (1.8°, 89.7°, 82.8°) and (1.8°, 90.4°, 19.4°) for the minority phase and the majority phase, respectively. The EBSD patterns show signal shielding at bottom.

[u v w] and (h k l) are the direction index and plane Miller index for the minority phase, respectively. [U V W] and (H K L) are the direction index and plane Miller index for the majority phase, respectively. A pair of parallel directions or planes in each phase can be calculated through the coordinate transformation matrices [M] and [M*] using the formulae below.

$$\begin{bmatrix} H \\ K \\ L \end{bmatrix} \parallel \left[M\right]^{-1} \begin{bmatrix} h \\ k \\ l \end{bmatrix}, \quad (2)$$

$$\begin{bmatrix} U \\ V \\ W \end{bmatrix} \parallel \left[M^{*}\right]^{-1} \begin{bmatrix} u \\ v \\ w \end{bmatrix}, \quad (3)$$

$$\left[M\right] = \left[M^{*T}\right]^{-1} = \left[M^{*-1}\right]^{T}, \quad (4)$$

Some typical orientation results are presented in Tables S3 and S4. The results from (0 0 1) and cross-section planes are consistent with each other. The Rodrigues vector in Table S4 means that the minority phase's **a** and **b** directions will coincide with the majority phase's **A** and **B** directions after rotating around the shared [0 0 1] axis about 63.4° clockwise, as shown in Fig. S3. As the phases have four-fold rotation symmetry around C or c axis, **B** in Fig. S3 can be labeled as **A** with new **B** in the opposite direction of **A** in Fig. S3. In this case, the minority phase's **a** and **b** directions will coincide with **A** and **B** directions after rotating around the shared [0 0 1] axis about 26.6º counter clockwise.

Table S3. Orientations of the majority phase P and minority phase S. The cross-section was prepared by FIB.

Location	Euler angles			Orientation matrix	
		P	S	[g_P]	[g_S]
(0 0 1) plane	ϕ	165°	165.5	-0.89303, 0.449232, 0.026338	0.001188, 0.99109, 0.133186

	1		°	0.448767, 0.884711, 0.126074	0.999407, -0.00576, 0.033949 0.034413, 0.133067, -0.99051
	Φ	172.6 °	172.1 °	0.033335, 0.124407, -0.99167	
	ϕ 2	11.8°	75.7°		
Cross-section of (0 0 1)	ϕ 1	1.8°	1.8°	0.94283, 0.02731, 0.332153 -0.33179, -0.01702, 0.9432	0.125108, 0.009129, 0.992101
	Φ	90.4°	89.7°	0.03141, -0.99948, -0.00698	-0.99165, -0.03051, 0.125332
	ϕ 2	19.4°	82.8°		0.03141, -0.99949, 0.005236

Table S4. Orientation relationship of the majority phase P and minority phase S. The cross-section was prepared by FIB. **C** or **c** axis is out of the paper, following the right-hand rule.

Location	Transformation matrix [M^*]	Rodrigues vector	Parallel directions
(0 0 1) plane	1.0205, 2.0384, -0.0199	[0 0 1], 63.4°	$[1\ 0\ 0]_P$ // $[1\ -2\ 0]_S$
	-2.0385, 1.0206, -0.0024		$[0\ 1\ 0]_P$ // $[2\ 1\ 0]_S$
	0.0029, 0.0082, 0.9899		$[0\ 0\ 1]_P$ // $[0\ 0\ 1]_S$
Cross-section of (0 0 1)	1.0207, 2.0382, -0.0276		$[1\ 2\ 0]_P$ // $[1\ 0\ 0]_S$
	-2.0384, 1.0207, -0.0035		$[-2\ 1\ 0]_P$ // $[0\ 1\ 0]_S$
	0.0040, 0.0114, 0.9898		$[0\ 0\ 1]_P$ // $[0\ 0\ 1]_S$

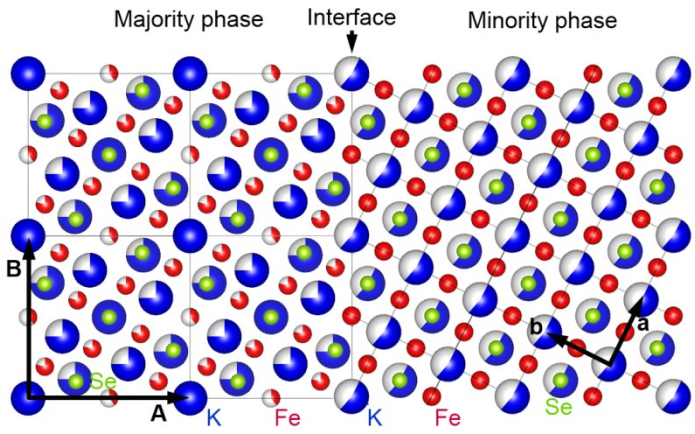

Figure S3. An illustration of orientation relationship between the two phases. Unite cells boundaries are indicated with grey lines. The majority phase is an ion-vacancy-ordered phase with a $\sqrt{5}\times\sqrt{5}\times1$ superstructure. The minority phase has a $ThCr_2Si_2$-type structure. The two phases share the same direction in c axis, but a and A axes have an angle of 63.6°. The unfilled portion of each atom represents vacancy occupancy.

The coordinate transformation matrices are close to rational forms, which indicates the two phases have nearly coherent interfaces.

$$\left[M^*\right] = \begin{bmatrix} 1 & 2 & 0 \\ -2 & 1 & 0 \\ 0 & 0 & 1 \end{bmatrix}, \text{ or } \left[M\right] = \begin{bmatrix} 1/5 & 2/5 & 0 \\ -2/5 & 1/5 & 0 \\ 0 & 0 & 1 \end{bmatrix}.$$

2. Determination of orientations of linear and planar features of the minority phase parallelepipeds by trace analysis

The minority phase S forms 3D architecture composed of parallelepipeds that lies in certain crystallographic planes and extend along certain directions. The traces of the planar feature are visible in any two of the X-Y and Z-X planes for the Cartesian sample frame, as shown in Fig. S4. The angle between the trace and the X axis is α in the Y-Z plane and β in the X-Y plane. The irrational unitless direction $\mathbf{r}_1$ of the trace in the Z-X plane is [-cosα, 0, -sinα]. The irrational unitless direction $\mathbf{r}_2$ of the trace in X-Y plane is [cosβ, sinβ, 0]. The plane normal is the cross product of $\mathbf{r}_1$ and $\mathbf{r}_2$. The normalized irrational plane normal **n**' is,

$$\mathbf{n}' = \frac{\mathbf{r}_1 \times \mathbf{r}_2}{|\mathbf{r}_1 \times \mathbf{r}_2|} = \frac{1}{\sqrt{\sin^2\alpha + \cos^2\alpha \sin^2\beta^2}} \begin{bmatrix} \sin\alpha\sin\beta \\ -\sin\alpha\cos\beta \\ -\cos\alpha\sin\beta \end{bmatrix} \quad (5)$$

The corresponding vector **n** with respect to the crystal basis is

$$\mathbf{n} = [\mathrm{T}]^{-1}[g]\,\mathbf{n}' \quad (6)$$

For an elongated parallelepiped, the Miller indices of all side planes of the parallelepiped phase can be calculated using the method above. The direction index of the elongation direction is the cross product of the two plane Miller indices.

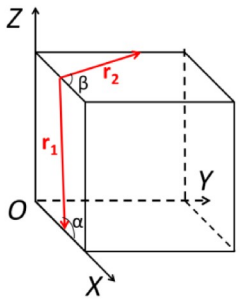

Figure S4. Planar feature traces (red) on the surfaces of an orthogonal material block which edges are along the sample frame basis vectors, **X**, **Y**, and **Z**. The directions of the traces are chosen such that the direction of the cross product $\mathbf{r}_1 \times \mathbf{r}_2$ is same as the plane normal, following the right-hand rule.

As shown in Fig. 3(c) of the article, α is about either 50° or 130°. From Fig. S1, β is about either 45° or 135°. These angles are used for traces analysis, which results are presented in Tables S5 and S6. It is clear that the parallelepipeds of the minority phase lies in its {1 1 3} planes and extends along its <3 0 1> directions. The {1 1 3} and <3 0 1> of the minority phase approximately corresponds to {-1 3 3} and <3 6 5> of the majority phase, respectively. For

reference, the plane and direction schematics are given in Fig. S5.

The trace-analysis results are consistent with the 3D reconstruction results. Note the 3D reconstruction volumes shown in the movies given in Supplementary Materials are in perspective views for better view of the 3D architecture. Measurements cannot be made near the volume edges where the images are heavily distorted, when performing trace-analysis using the 3D volumes.

Table S5. Determination of the crystallographic planes that the minority phase parallelepipeds lie in by trace analysis.

Plane Miller index	(α, β)			
	(50°, 45°)	(130°, 45°)	(50°, 135°)	(130°, 135°)
(h k l): irrational	0.29, -0.29, -0.9111	0.29, -0.29, 0.91	0.29, 0.29, -0.91	0.29, 0.29, 0.91
(h k l): rational	(1 -1 -3)	(1 -1 3)	(1 1 -3)	(1 1 3)

Table S6. Determination of the crystallographic directions that the minority phase parallelepipeds extend along by trace analysis.

Side plane #1	Side plane #2	Parallelepiped direction
(1 -1 -3)	(1 1 -3)	[3 0 1]
	(1 1 3)	[0 -3 1]
(1 -1 3)	(1 1 -3)	[0 3 1]
	(1 1 3)	[-3 0 1]

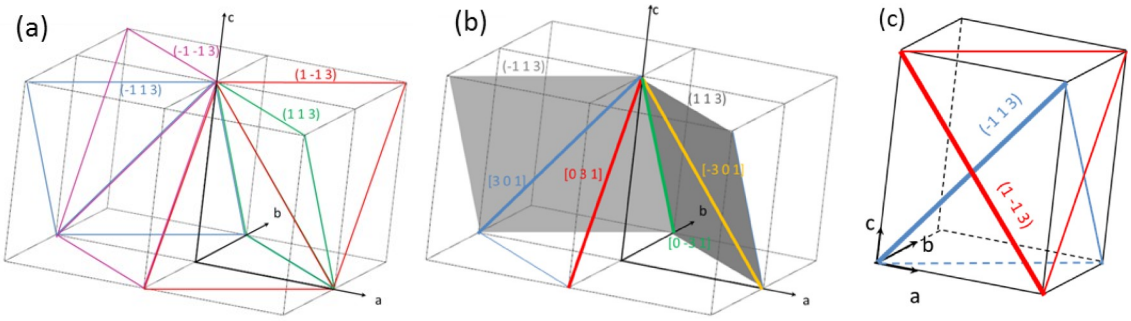

Figure S5. {1 1 3} planes and <3 0 1> directions of the minority phase. (c) shows the traces of two {1 1 3} planes on (0 1 0) or a-c plane can form an "X" shape, as observed by FIB-SEM.

References

1. D. P. Shoemaker, D. Y. Chung, H. Claus, M. C. Francisco, S. Avci, A. Llobet, and M. G. Kanatzidis, Phys. Rev. B **86**, 184511 (2012).
2. G. Nozle, Ultramicroscopy **107**, 172 (2007).

Movies

Movie 1. 3D microstructure of pseudo-single-crystal $K_xFe_{2-y}Se_2$ in a volume of $16 \times 10 \times 10$ μm^3.

Movie 2. 3D microstructure of pseudo-single-crystal $K_xFe_{2-y}Se_2$ in a volume of $4 \times 4 \times 4$ μm^3, in which the volume fraction of the superconducting phase is 11.5%. The extra blue phase comes in at 0.8-1% depending on cropping, which is identified impurity phase.

Movie 3. 3D microstructure of pseudo-single-crystal $K_xFe_{2-y}Se_2$ in a volume of $2 \times 2 \times 2$ μm^3, in which the volume fraction of the superconducting phase is 10.2%. The extra blue phase comes in at 0.8-1% depending on cropping, which is identified impurity phase.